

Binary optic reflection grating for an imaging spectrometer

Daniel W. Wilson, Paul D. Maker, and Richard E. Muller

Center for Space Microelectronics Technology, Jet Propulsion Laboratory
California Institute of Technology, Pasadena, CA 91109

ABSTRACT

A single optical element capable of both wavelength dispersion and imaging would be useful for implementing compact imaging spectrometers. We have fabricated a hybrid refractive/diffractive element that accomplishes these goals. The element is a plano-convex glass lens with a reflective diffractive surface fabricated on the planar side. The diffractive surface combines a blazed grating and several forms of aberration correction. The surface relief profile was fabricated in poly-methyl methacrylate (PMMA) by direct-write electron beam (E-Beam) lithography followed by a single development step. The 8.2 mm x 8.2 mm exposure pattern was corrected for both the nonlinear dose response of the PMMA and the E-beam proximity effect. Surface characterization by atomic force microscopy revealed that the grating blaze profile was linear, although the grating was overetched. Optical characterization included diffraction efficiency measurements, knife-edge spot size measurements, and 1D spot irradiance profiles at multiple wavelengths and field positions. The measured spot and field sizes translate to a resolution of 65 wavelength channels in the 400 to 700 nm band of interest and 128 spots along the imaging direction for a 10 mm entrance slit.

Keywords: diffractive optics, binary optics, hybrid optical elements, gratings, imaging spectrometer, electron-beam lithography

1. INTRODUCTION

Diffractive optical elements (DOEs) have found increased application as design and fabrication methods have improved in recent years. DOEs display unique properties that can be utilized either independently or together with traditional refractive elements to enhance the performance and/or mechanical properties of optical systems. In this paper, we describe a single hybrid refractive/diffractive element that could serve as the central element in an imaging spectrometer. Such a spectrometer would be lightweight, rugged, and compact necessary attributes for miniature flight vehicles. In addition, the reflective element could potentially be replicated in plastic for low cost. When combined with a low cost front-end imaging/scanning system and a charge-coupled device (CCD) focal plane array (FPA), throw-away spectrometers for single-use operation may become feasible. Figure 1 illustrates the hybrid optical element and its functionality in an imaging spectrometer. The slit samples an image of a scene, and the hybrid element disperses and reimages the information onto a focal plane array. Ultimately, the image of the scene would be scanned across the slit, and the spectral and spatial data from the FPA would be clocked out synchronously. The hybrid optical element is a combination of a plano-convex refractive lens and a diffractive grating and aberration corrector. fabrication of the grating/aberration corrector was accomplished in poly-methyl methacrylate (PMMA) by a single-step electron-beam direct write followed by development and aluminum coating. The details of the design, fabrication, surface characterization, and optical testing of the element are discussed in this paper.

2. DESIGN

The design of the refractive/diffractive element aimed to meet the following goals. Assuming a 10 mm high entrance slit, the slit was to be dispersed and imaged onto a 10 mm square focal plane array. The desired wavelength band was 400-700 nm. To provide enough dispersion and clearance for the FPA, it was decided that the center wavelength, 550 nm, should be diffracted to the center of the FPA located approximately 20 mm from the entrance slit. The element was tilted by 2° so that the zeroth order would not fall on the entrance slit. This tilt also increased the required grating period, easing fabrication, but decreased the dispersion. The imaging power was provided mostly by the refractive element. For this first attempt, we decided to set the distance from the slit to the grating to be 100 mm, and hence a plano-convex BK7 glass lens of focal length 100 mm was chosen (Newport KPX 094). For the initial grating design, it was assumed that the lens

produces ideal plane waves incident on the grating. The ideal grating reflectance as a function of position y is $r(y) = \exp[i\Phi(y)]$, where the phase $\Phi(y) = k(\sin\theta_d + \sin\theta_{inc})y$, $k = 2\pi/\lambda$, $i = (-1)^{1/2}$, θ_{inc} is the incident angle, and θ_d is the desired first-order diffraction angle. For the configuration described above, the incident angle was 2° , and the diffracted angle was required to be 9.3° . However, because the diffraction occurs inside the PMMA ($n = 1.49$), Snell's law reduces these angles to $\theta_{inc} = 1.34^\circ$ and $\theta_d = 6.23^\circ$, and the wavelength decreases to $\lambda = \lambda_0/n$, where λ_0 is the freespace wavelength. The depth of the grating profile is then given by $d(y) = \lambda[\Phi(y) \bmod 2\pi]/4\pi$. Hence the maximum depth is only half of the wavelength in the PMMA 184 nm for $\lambda_0 = 550$ nm. This is advantageous because surface roughness becomes a significant problem for deep profiles. To fabricate this grating using 193-nm beam lithography, we pixelized the depth profile into 0.5 μm square areas having constant depths. This changes the linear blaze into a staircase blaze and shifts the transition points slightly. To investigate the influence of this pixelization and other fabrication errors on the grating efficiency, Fourier optics modeling was performed. Because this approach does not properly treat the surface relief boundary conditions, the results are only approximate. Assuming an incident plane wave, $U_{inc}(y) = \exp(ik \sin\theta_{inc} y)$, the diffracted angular spectrum of plane waves is $A(v) = F\{U_{inc}(y)\} / F\{r(y)\}$, where $F\{\}$ denotes the Fourier transform and $v = \sin\theta/\lambda$ is the spatial frequency along the y direction. The reflectance is that calculated directly from the depth profile, $r'(y) = \exp[i\Phi'(y)]$, $\Phi'(y) = 4\pi d(y)/\lambda$. Figure 2 shows a plot of the efficiency $\eta = |A(\theta_d(\lambda))|^2 \cos\theta_d / \cos\theta_{inc}$ for the zeroth, first, and second diffracted orders for $\lambda_0 = 400$ to 700 nm.

The design and modeling described above addressed the dispersive performance of the grating. To investigate and improve the imaging performance, ray tracing was required. To allow close watch over the tracing and optimization process, code was written in MATLAB to perform the tracing. Commercial optical design software could also have been used. In standard fashion, where a ray intersected a refractive surface, tangential wavevector matching, was used to find the ray direction in the second medium (Snell's law). Where a ray intersected a diffractive surface, the local grating vector \mathbf{K} was found from the gradient of the diffractive element's phase function, $\mathbf{K} = \nabla\Phi$ (the local grating period is $2\pi/|\nabla\Phi|$). If the diffractive surface was tilted, \mathbf{K} was tilted so as to be tangential to the surface. The vector Floquet condition was then used to find the Floquet wavevectors $\mathbf{o}_m = \mathbf{k}_{inc} - m\mathbf{K}$ inside the locally periodic medium, where \mathbf{k}_{inc} is the incident wavevector inside the medium and m is the integer diffraction order. The forward or backward diffracted wavevectors were found by matching to the tangential components of \mathbf{o}_m .

Using this technique, rays were traced from the slit through the tilted lens with a reflective diffractive back surface. Initially, the diffractive surface was composed of only the linear grating phase term

$$\Phi_{\text{grat}}(x, y) = k(\sin\theta_d + \sin\theta_{inc})y, \quad (1)$$

where x, y lie in the tilted coordinate system of the lens. Ray tracing through this system revealed severe aberrations and a tilted image field (blue focused closer to the lens than red due to the natural dispersion of BK7). With the E-beam lithography fabrication technique, we are not limited to linear phase functions. Hence additional phase terms can be added to attempt to correct for the aberrations. As opposed to trying to correct for all aberrations at once with a very general phase function, individual terms were added to correct for specific aberrations. The simplest correction was to use the negative dispersion of a radially symmetric Fresnel lens phase function to correct for the chromatic aberration (tilted image field). The lens phase function that was used was

$$\Phi_{\text{Fresnel}}(x, y) = k \left(\sqrt{f_{\text{Fresnel}}^2 + x^2 + y^2} - f_{\text{Fresnel}} \right), \quad (2)$$

where $r^2 = x^2 + y^2$ and $f_{\text{Fresnel}} = 4000$ mm is the focal length of the diffractive lens. This phase function was doubled to account for the double pass through the lens. The focal length was adjusted until the positions of best focus for each color nominally fell in a plane that was parallel to the plane containing the slit. In retrospect, better imaging performance may have been achieved if the image plane had been tilted toward the ray normals. The next obvious correction was spherical aberration. The phase function for this correction is derived from the difference between the phase of a perfect Fresnel lens [Eq. (2)] and that of a thin spherical lens. The phase function of a thin spherical plano convex lens is

$$\Phi_{\text{splens}}(x, y) = k_0 [n_{\text{lens}}(\lambda_0) - 1] \Lambda(x, y), \quad (3)$$

where $\Lambda(x, y) = (R^2 - x^2 - y^2)^{1/2} - (R^2 - x_m^2 - y_m^2)^{1/2}$, with $R = 51,68$ mm (front surface radius of curvature) and $x_m = y_m = 5$ mm (maximum distance from origin). The corrector phase function should add to Eq. (3) to produce the perfect phase function, thus

$$\Phi_{\text{corrector}}(x, y) = \left(k \sqrt{f_{\text{Fresnel}}^2 + x^2 + y^2} - f_{\text{Fresnel}} \right) - k_0 [n_{\text{lens}}(\lambda_0) - 1] \Lambda(x, y). \quad (4)$$

This phase function was also doubled to account for the double pass through the lens. The focal length $f_{s.a.cor} = 98.7$ mm was adjusted to minimize the root mean square (rms) spot size at the design wavelength. Figure 3 shows a plot of $\Phi_{s.a.cor}$. Finally, in an attempt to correct for tilt and higher order aberrations, a polynomial phase function was added,

$$\Phi_{poly}(x, y) = k(Ar^2y + Bx^2), \quad (5)$$

with $A = 3.78 \times 10^{-6} \text{ mm}^{-2}$ and $B = 2.47 \times 10^{-5} \text{ mm}^{-1}$. Figure 4 shows a plot of Φ_{poly} . The first term corrects for some of the tilt aberration and the second term added power in the vertical direction to correct for observed astigmatism. The coefficients A and B were found by using MATLAB's built-in simplex optimization routine with the rms spot size as the merit function. Various other polynomials were tried, but adding more terms tended to cause the optimization routine to find local minima where the performance was actually worse. The total phase function used for the final diffractive element was

$$\Phi_{tot} = \Phi_{grat} + 2\Phi_{c.a.cor} + 2\Phi_{s.a.cor} + \Phi_{poly}. \quad (6)$$

If a global optimization routine were available, a better approach would have been to keep the grating term, add a radially symmetric parabolic term to adjust the tilt of the image field, and then add a general polynomial of the form $\sum A_{pq}x^p y^q$ will), even, to optimize the imaging performance. Several commercial ray tracing programs have the capability to model such phase functions and perform optimization. Figure 5 shows a three dimensional view of rays traced through the element from the center of the slit at wavelengths 400, 550, and 700 nm. Figure 6 shows a top view of the focal region of rays at wavelengths 400, 475, 550, 625, 700 nm, and with a denser ray grid. It shows that the field curvature will limit the performance. Figure 7 shows the spot diagram in the best focal plane for 5 different object points along the height of the slit. The average rms spot size was $\sim 54 \mu\text{m}$. This indicates that a resolution of ~ 180 spots in the vertical (imaging) direction and ~ 120 spots in the lateral (wavelength) direction would be possible.

3. PATTERN PHOTOLITHOGRAPHY AND FABRICATION

Once the diffractive surface phase function was determined, the desired depth profile was given by $d(x, y) = \lambda_0 [\Phi_{tot}(x, y) \bmod 2\pi] / 4\pi n$ where $\lambda_0 = 550 \text{ nm}$ is the design wavelength, and $n = 1.49$ (PMMA). This function was sampled into $0.5 \mu\text{m}$ square pixels to create a pattern of $16K \times 16K$ pixels ($K = 1024$). Hence the total size of the diffractive surface was $8192 \mu\text{m} \times 8192 \mu\text{m}$. Some details of the fabrication technique will be presented here, and more information can be found in Refs. 2-8. Before Ti-beam writing the pattern in PMMA, several pattern preparation steps had to be carried out. First, the depth data had to be converted to Ti-beam dose data. We have measured the dose response of PMMA on quartz substrates and have found that for 10 seconds of development in pure acetone, the amount of PMMA removed is given by the exponential, $\text{depth} = B[\exp(\text{dose}/C) - 1]$, where $B = 0.22 \pm 0.01 \mu\text{m}$, $C = 70 \pm 1.5 \mu\text{C}/\text{cm}^2$. Next, the dose data had to be corrected for the Ti-beam proximity effect exposure resulting from electrons back-scattered from underlying PMMA and from the substrate. This is a very necessary correction. For our 50 keV electron beam, fully one-third of the exposure dose results from such back scatter in any uniformly exposed area larger than $20 \mu\text{m}$ square. The proximity effect is commonly described by a Gaussian model for the dose deposition function $D(r) = \delta(t) + (\eta/\pi\alpha^2) \exp(-r^2/\alpha^2)$. We have characterized this effect by exposing and developing rectangular regions, and then profiling the depth with an atomic force microscope. For PMMA on quartz, the measurements indicated that the proximity effect range $\alpha = 8.5 \pm 0.2 \mu\text{m}$ and the amplitude $\eta = 0.5 \pm 0.05$. For a primary Ti-beam dose pattern described by $S(r)$, the actual exposure dose experienced by the PMMA will be $P(r) \otimes D(r)$ where \otimes represents 2-D convolution. The effect of the proximity dose can be completely compensated for by delivering a modified pattern dose, $P'(r)$ calculated such that $P(r) = P'(r) \otimes D(r)$. The proximity effect correction required that a $16K \times 16K$ deconvolution be performed to determine $P'(r)$ for the grating/aberration corrector. This proved to be rather challenging. A special fast Fourier transform routine was written that utilized disk storage to handle pixel patterns up to the required $16K \times 16K$. The code was developed and executed on a 90 MHz Pentium PC with 32 Mbytes of RAM. For smaller patterns that fit entirely in RAM, the code was very efficient a $1K \times 1K$ deconvolution took only 1.2 minutes. For the $16K \times 16K$ pattern, however, the deconvolution took 22.5 hours and required a 1.2 Gbyte temporary disk file. After deconvolution, the doses are binned into 64 levels as limited by the Ti-beam pattern generator, and written in the format (called JI-DJ51) required by the JEOL pattern generator. In that format, 16 bytes of data are needed to describe each pixel to be exposed. In allocating the 64 available exposure doses, bins having equal etch-depth steps were chosen. For the $16K \times 16K$ pattern, a JEOL51 file 375 MB long was generated.

The lens was prepared for writing by spinning in succession five layers of PMMA onto the planar surface. Each deposition sequence included a bake-out for 60 minutes at 170°C . This results in a total film thickness of approximately 2.5

μm much thicker than required, but the same thickness as was used for proximity effect calibration. Prior to exposure, the sample was overcoated with 200 Å of aluminum which acted as a discharge layer, preventing defocusing due to surface charge buildup. The pixel pattern was then written using the JEOL JBX-5DII electron beam tool operating at 50 keV in its low resolution 4th lens mode. The field size the distance spanned by deflection of the beam without need for stage motion was 512 μm , and at 1 nA current, the beam waist was of the order of 0.1 μm . Individual 0.5 μm square pixels were exposed by rastering this beam in steps of 0.05 μm , back and forth, with the delay time between steps adjusted to give the desired dose. This rastering, timing, and positioning were handled automatically by the JBX-5DII once given the coordinates and desired exposure for the pixel. The 1- μm beam exposure of the grating/aberration corrector took approximately 10.5 hours. After exposure, the aluminum overcoat was removed with dilute AZ 400K photoresist developer and the film was developed in pure acetone for 10 seconds. This was accomplished using a Solitec spinner equipped with an electronically controlled Tridac resist dispenser. The lens was spun at 1000 RPM while the acetone was squirted down at the center of rotation. At the end of the 10 seconds, the acetone was abruptly cut off and replaced by a blast of dry nitrogen which quenched the development and at the same time dried the surface of the PMMA. Finally, an aluminum coating 2000 Å thick was evaporated onto the film to provide high reflectivity.

4. SURFACE CHARACTERIZATION

After fabrication, the surface was inspected with an optical microscope, a scanning electron microscope (SEM), and profiled with an atomic force microscope (AFM). optical inspection at 1000 \times revealed no major flaws in the element, but the 1- μm beam field boundaries were visible. 1- μm beam field stitching errors can be a significant problem for large area exposures, but the SEM inspections showed that the field stitching error was at most half of a pixel (0.25 μm) for the outermost fields. Figure 8 shows an AFM scan of approximately 5 periods of the surface near the corner of the pattern. The offsets in the grating steps are due to the presence of the aberration correction phase function. Figure 9 is a cross section of the scan showing the grating profile. The blare appears linear, indicating that the proximity effect correction worked well. However, the maximum depth is approximately 230 nm approximately 25% deeper than the desired depth of 184 nm. This means that the grating should have maximum efficiency for 685 nm rather than 550 nm. Possible explanations for the depth error are changes in developer temperature and aluminum overcoat thickness between calibration runs and the production run. The different substrate (BK7 rather than fused quartz) may have also played a role. The AFM scan also shows surface roughness which will cause diffuse scattering. The center facet in Fig. 8 was fit to a plane and the rms roughness was calculated to be $p \approx 10$ nm. When substituted into an approximate formula for total integrated scattering,⁹ $TIS = (4\pi p / \lambda)^2$, this predicts a scattering fraction of about 5% at 550 nm.

5. OPTICAL TESTING

5.1. Efficiency measurements

Several optical tests were carried out to characterize the device performance. The diffraction efficiency was measured by focusing a 633 nm HeNe laser beam to a spot and allowing the beam to expand and slightly underfill the grating. The position of the focal spot was approximately in the slit position. The power in the incident beam and the diffracted orders were measured using a photodiode detector. Table 1 shows the measured diffraction efficiencies. The first order efficiency was ~66%, and all the other orders had very low efficiency. The high preferential diffraction into the first order for 633 nm is a result of overetching the grating. Antireflection coating the lens would have likely increased the first order efficiency by ~8%.

5.2 Knife-edge spot size measurements

Imaging performance was also investigated using the HeNe laser. The beam was again focused to a small spot in the slit position and the element was carefully aligned according to the design. The beam focusing lens for this test was of higher power, causing the expanding beam to overfill the grating. Knife-edge tests were then performed on the initial beam focus (acting as a point source) and the first-order diffracted focal spot. This was accomplished by scanning a razor blade across the focal spot using a motorized micrometer and recording the transmitted power on a chart recorder. Scans in both the vertical and horizontal directions were performed. To investigate the performance along the length of a 10 mm high

Table 1. Measured diffraction efficiencies

Order	Measured Efficiency
-4	0.36 %
-3	0.48 %
-2	0.48 %
-1	0.60 %
0	0.96 %
1	66.3 %
2	0.84 %
3	0.24 %
Air-glass reflection, higher orders, and diffuse scattering	29.7 %

entrance slit, the system was realigned to simulate point sources at 5 mm above and below center. Table II summarizes the results. The values quoted are the widths that contain 80/0 of the transmitted twain energy. This test slightly underestimates the spot size because an integration of the irradiance parallel to the knife-edge is inherent in the measurement. Nevertheless, the spot sizes were encouraging. For an image height of ~10 mm, the vertical spot widths would support a resolution of ~150 spots. However, this test was performed at a single wavelength, and as discussed in Sec. 2, the field curvature will degrade the performance.

Table II. Knife-edge measured spot sizes (quoted widths contain 80 % of beam energy)

spot	Horizontal (y or λ) Width	Vertical (x) Height
Input	13 μm	18 μm
Top of image field(+5 mm)	66 μm	57 μm
Center of image field(0 mm)	62 μm	40 μm
Bottom of image field(-5 mm)	76 μm	66 μm

5.3. Multiple wavelength spot profile measurements

To investigate the performance over the wavelength band of interest (400-700 nm) and at multiple field positions, a monochromator and CCD camera were used as shown in Fig. 10. A 10 μm core optical fiber was inserted into the exit slit of the monochromator and the other end was used as the point source to test the lens/grating spectrometer element. The system was aligned as closely as possible to the design specifications, and then the CCD detector was positioned to find the best focal plane. The defocused zeroth order was observed to have a dark square region in the center, indicating that the grating was overfilled as desired. The first order focal spot irradiance distributions were captured using a frame grabber and NIH Image software running on a Macintosh IIx. Focal spots at wavelengths 400, 475, 550, 625, and 700 nm were taken for input spot vertical positions of $x = 0, \pm 2.5, \pm 5$ mm to simulate the 10 mm entrance slit. The efficiency of the grating at 400 nm was quite low due to the grating overdevelopment. A montage of the measured irradiance distributions is shown in Fig. 11. There is a one-to-one correspondence between the spots shown in Fig. 11 and those in the spot diagram of Fig. 7. However, the distance between the spots in the Fig. 11 does not represent the actual distance between the spots on the CCD. The width of the field in the wavelength direction was 6.75 mm, which is slightly larger than the predicted width of 6.54 mm. The spots showed more aberration in the wavelength direction than in the imaging direction all have a tail towards longer wavelengths. These aberrations are somewhat worse than predicted (compare to Fig. 7). Calibration measurements determined that each pixel in the irradiance distributions represents approximately a 13 $\mu\text{m} \times 13 \mu\text{m}$ area. Quantitative analysis of the spot data has not been performed, but inspection indicates that most of the energy in the spots is contained

within an 8 pixel wide by 6 pixel high area. This corresponds to spot sizes of $104\mu\text{m} \times 78\mu\text{m}$. Considering the size of the image field, this translates into a resolution of 65 wavelength (lateral) spots ($\Delta\lambda \approx 5\text{ nm/spot}$) \times 128 image (vertical) spots.

6. CONCLUSION

overall, our effort to design and fabricate an element that performed both wavelength dispersion and imaging was successful. The design may have been improved by tilting the focal plane toward the lens and including a more general aberration correction phase function. Fabrication could have been improved by using an antireflection coated lens and calibrating the I-beam proximity effect for PMMA on BK7 glass. If PMMA is not durable enough for the environment of operation, then either an etching process to transfer the profile into the substrate⁷ or replication in a high durability plastic could be implemented.

7. ACKNOWLEDGMENTS

We gratefully acknowledge Thomas Chrien, Michael Eastwood, and Gregory Bearman for allowing us to use the test equipment and facilities of the Airborne Visible/Infrared Imaging Spectrometer (AVIRIS) laboratory at Jet Propulsion Laboratory.

The research described in this paper was performed by the Center for Space Microelectronics Technology, Jet Propulsion Laboratory, California Institute of Technology. Funding was provided by the Ballistic Missile Defense Organization / innovative Science and Technology office, the National Aeronautics and Space Administration / Office of Space Access and Technology, and by the Jet Propulsion Laboratory Director's Research and Development Fund.

8. REFERENCES

1. J. Goodman, *Introduction to Fourier Optics*, chaps. 3-5, McGraw-Hill, New York, 1968.
2. T. Fujita, T. Nishihara, and J. Koyama, "Fabrication of micro lenses using electron-beam lithography," *Opt. Rev.* **6**, 613-615, 1981.
3. M. Ekberg, M. Larsson, S. Hård, and B. Nilsson, "Multilevel phase holograms manufactured by electron beam lithography," *Opt. Lett.* **15**, 568-569, 1990.
4. M. Larsson, M. Ekberg, F. Nikolajeff, and S. Hård, P. D. Maker, and R. E. Muller, "Proximity-compensated kinoforms directly written by I-beam lithography," *SPIE Proceedings Vol. CR49*, July 1993.
5. P. D. Maker, and R. E. Muller, "Phase holograms in poly methyl methacrylate," *J. Vac. Sci. Technol.* **11**, 2516-2519, Nov/Dec 1992.
6. P. D. Maker and R. E. Muller, "I-beam holograms in PMMA with proximity effect correction," *NASA CP-3227*, 207-221, Feb. 1993.
7. W. Daschner, M. Larsson, and S. Hård, "Fabrication of monolithic diffractive optical elements by the use of I-beam direct write on an analog resist and a single chemically assisted I-beam etching step," *Appl. Opt.* **34**, 2534-2539, 1995.
8. P. D. Maker, D. W. Wilson, and R. E. Mullet, "Fabrication and performance of optical interconnect analog phase holograms made by electron beam lithography," *SPIE Proceedings Vol. 1126*, to be published.
9. J. M. Bennett and L. Mattson, *Introduction to Surface Roughness and Scattering*, pp. 25, optical Society of America, Washington, D.C., 1989.

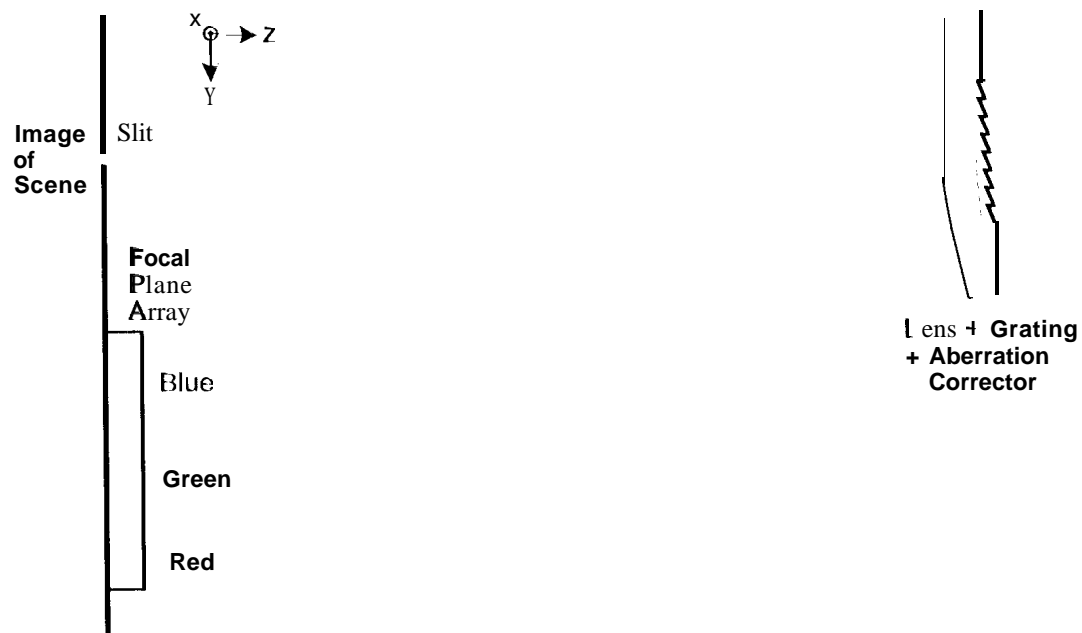


Figure 1. Illustration of hybrid refractive/diffractive element functioning as the focusing and dispersing element in an imaging spectrometer.

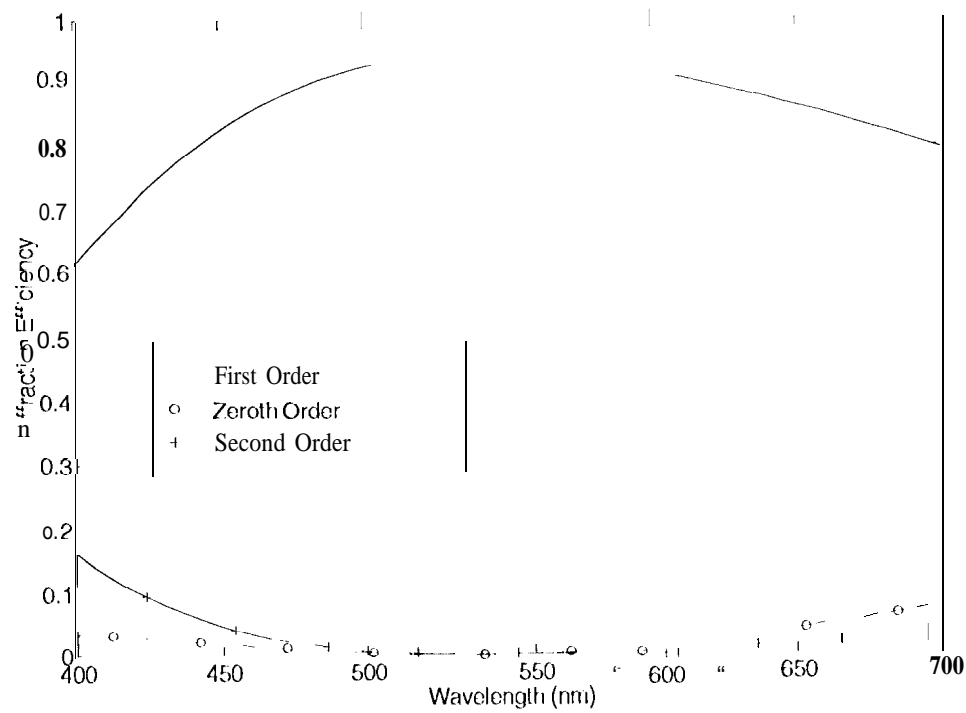


Figure 2. Approximate diffraction efficiencies for the pixelized grating profile. Efficiencies were calculated from the Fourier transform of the ideal reflectance.

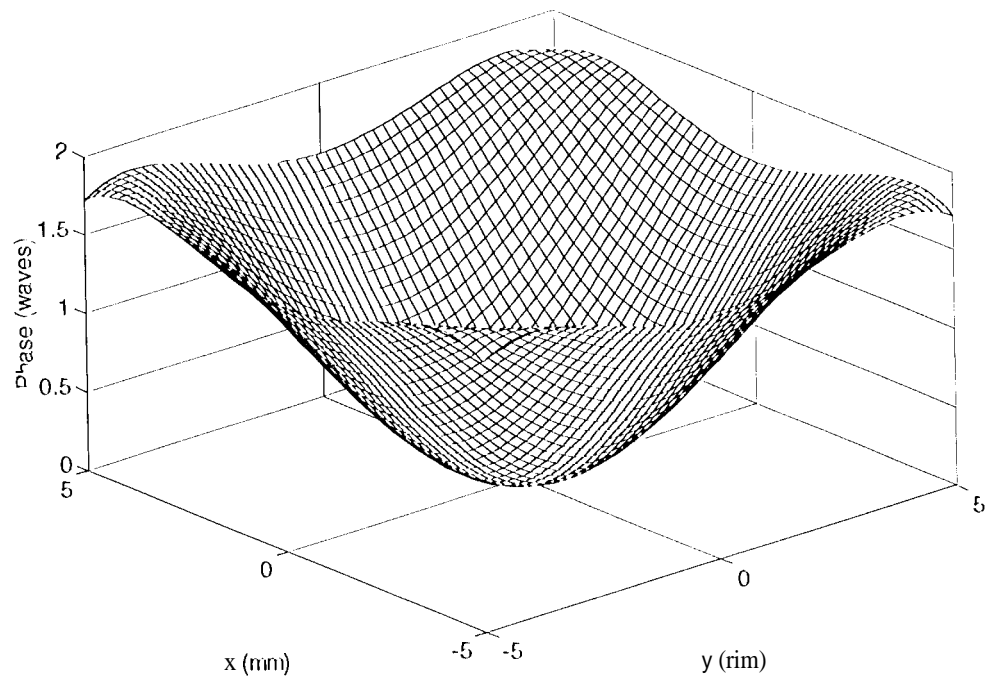


Figure 3. Spherical aberration correction phase function.

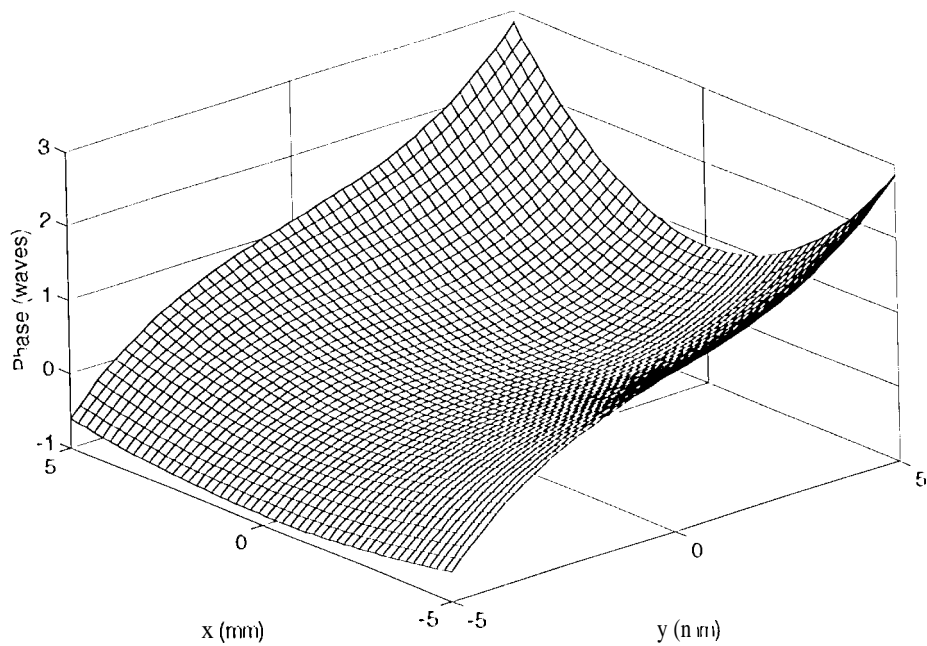


Figure 4. Polynomial **aberration** correction phase function.

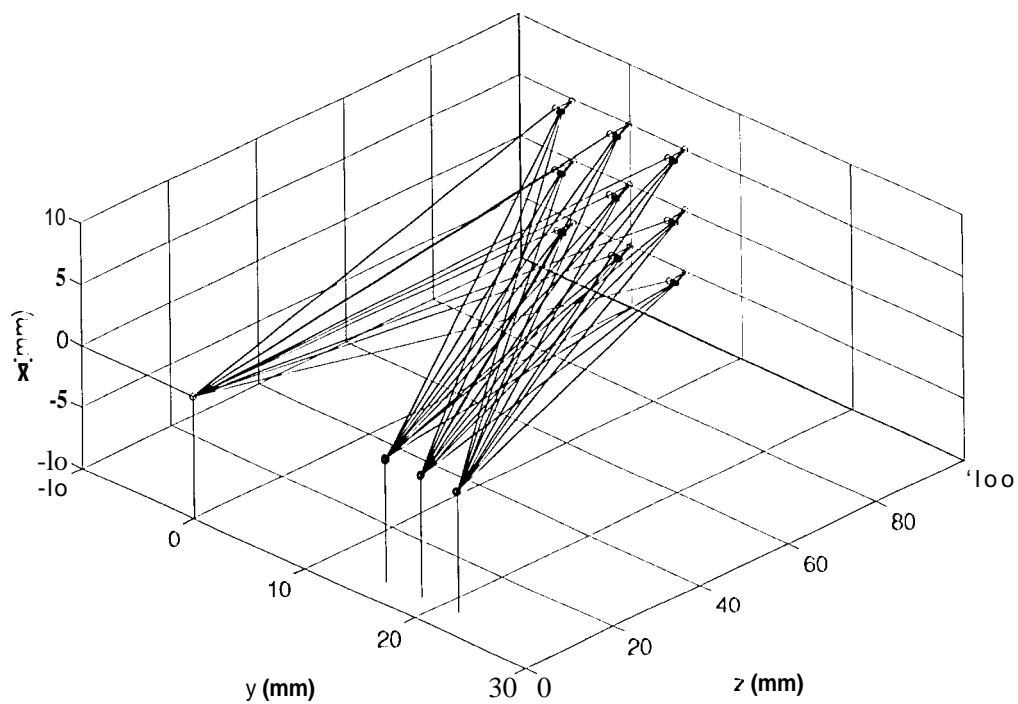


Figure 5. Rays traced from center of slit to the focal plane ($z = 6$ mm) for λ 400, 550, and 700 nm.

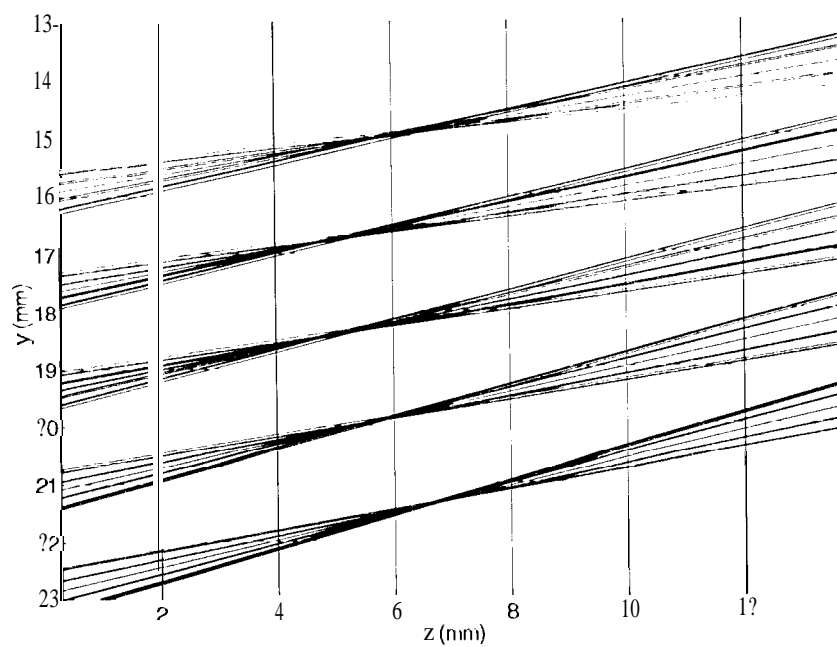


Figure 6. Top view of rays traced from center of slit through focal region for $\lambda = 400, 475, 550, 625,$ and 700 nm (top to bottom).

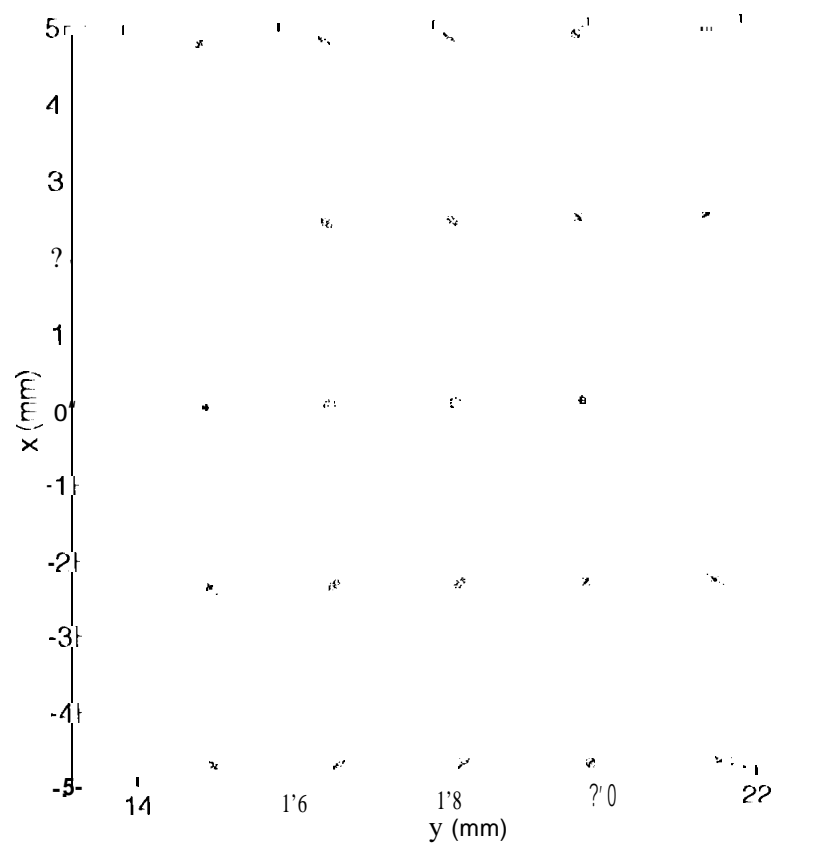


Figure 7. Focal plane spot diagram for object points $x = 0, \pm 2.5, \pm 5$ mm and wavelengths $\lambda = 400, 475, 550, 625, 700$ nm (left to right).

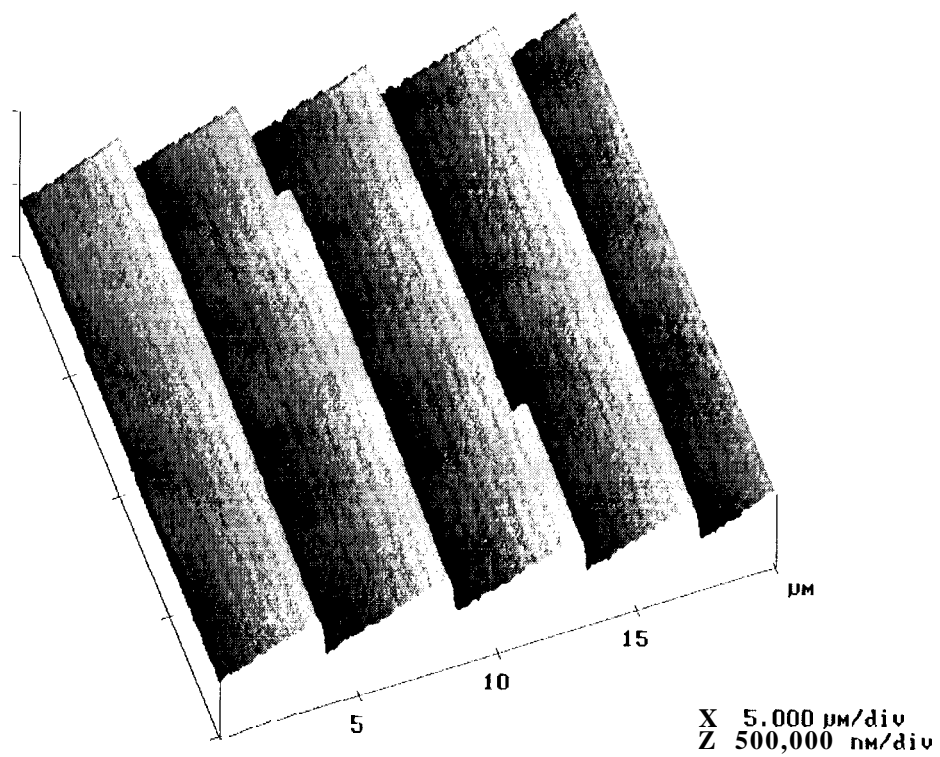


Figure 8. Atomic force microscope scan of the diffractive surface near a corner of the pattern. Offsets in the grating steps are due to the presence of the aberration correction phase function.

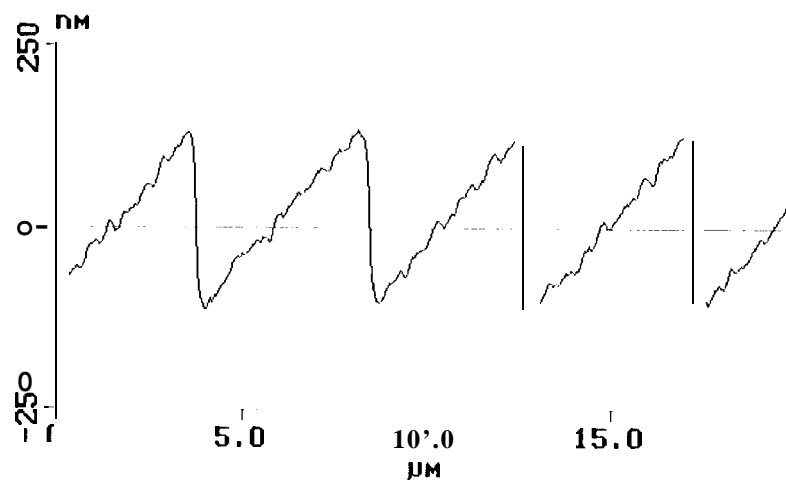


Figure 9. Cross section of Fig. 8. Maximum etch depth is ~ 230 nm. RMS roughness of the center facet (fit to a plane) is ~ 10 nm.